J. Electrochem. Sci. Eng. **15(4)** (2025) 2709; http://dx.doi.org/10.5599/jese.2709

Open Access : : ISSN 1847-9286
www.jESE-online.org

Original scientific paper

In situ electrochemical impedance spectroscopy of TiN-based hard coatings

Izabela Martinez✉ and Božidar Matijević

Faculty of Mechanical Engineering and Naval Architecture, University of Zagreb, Ivana Lučića 5, 10000 Zagreb, Croatia

Corresponding author: ✉*izabela.martinez@fsb.unizg.hr; Tel.: +385-1-6168-596*

Received: March 11, 2025; Accepted: May 2, 2025; Published: May 12, 2025

Abstract

Hard coatings are thin, wear-resistant films, typically composed of ceramic or metal-based compounds, that enhance surface durability and corrosion resistance. Advancing hard coatings depends on incremental improvements driven by extensive experimentation, which could be significantly enhanced by a fast, reliable, and non-destructive method for assessing coating barrier efficiency. A previously developed electrochemical impedance spectroscopy (EIS) press-on cell with a chloride-free, pH-neutral paste electrolyte, originally validated on stainless steel, bronze, coated bronze, and Corten steel, was adapted to determine barrier effectiveness of four coating/substrate combinations (TiN/TiCN and TiN/TiBN on 42CrMo4 and 32CrMoV12-10 steels) produced via plasma-assisted chemical vapor deposition and characterized by glow discharge optical emission spectroscopy and scanning electron microscopy (SEM). Impedance spectra were evaluated by equivalent circuit fitting, and the contributions of resistive and capacitive elements were analysed in detail. SEM image analysis using statistical features and binarization revealed an inverse relationship between grain boundary density and total coating resistance across the barrier spectrum, from ~kΩ cm² to ~MΩ cm². The EIS results aligned with literature data for similar hard coatings in neutral electrolytes, supporting the method's validity. The paste electrolyte method enables rapid, non-destructive screening of coatings with distinct barrier properties, offering a practical alternative to conventional destructive techniques.

Keywords

Plasma-assisted chemical vapor deposition; coating barrier efficiency; paste electrolyte; impedance spectra

Introduction

The importance of hard coatings in modern industrial applications is widely recognized. They are typically composed of ceramic or metal-based compounds (*e.g.* TiN, TiCN, TiBN) and enhance metallic and non-metallic substrates by improving resistance to abrasive and adhesive wear, erosion, scratching, chipping, heat, corrosion, and chemicals. Additionally, they provide biocompa-

tibility, aesthetic appeal, and protection under extreme conditions [1-3]. The benefits of using hard coatings include increased functionality and durability of consumer products for the end user and increased productivity and energy efficiency of the production process for manufacturers.

In many aggressive environments, hard coatings are chemically inert [4] and, with a typical thickness of ~3.0 μm [5] provide a barrier to the environment that protects the underlying metallic substrate from corrosion. The chemical inertness of the hard coating is attributed to its inherent chemical stability and coverage by a passive layer. For example, the exceptional chemical stability of TiN coatings is explained by a mixture of metallic, covalent and ionic bonds [6] as well as a nitrogen-enriched surface layer with a high electron density that prevents the migration of Ti^{3+} to the phase boundary [4,7]. Despite the stability, when exposed to oxygen, TiN is covered by a 1-2 nm thick passivating top layer [8] with titanium in an oxidation state between TiN and TiO_2 [9]. X-ray photoelectron spectroscopy shows that spontaneous passivation of the sputter-cleaned sample occurs at room temperature and a mixed oxynitride/oxide overlayer is detected after one day of exposure remains on the surface after one year of exposure, with more intermediate species Ti(N,O) present but without complete conversion to TiO_2 [6]. In ternary and quaternary titanium-based hard coatings, the composition of the oxide layer varies in accordance with the phases present [10].

The decisive factor for the corrosion protection ability of a chemically inert hard coating is its integrity, which can be impaired by pores that form during the deposition process or after a chemical or mechanical attack. Vapor-deposited transition metal nitride coatings regularly exhibit microscopic pores, pinholes, and/or voids [8,11], and the causes of these defects are well documented [12]. Titanium nitride coatings have a crystallographic structure consisting of faceted columns perpendicular to the surface with micro- and nanopores running between the columns and throughout the coating thickness [7,13,14]. The corrosive electrolyte penetrates the coating through the pores and encounters the electrochemically active areas of the substrate, leading to corrosion. Due to the inertness and passivity of the coating, corrosion mainly occurs in the base material [5,15]. In addition, the hard coatings are electrically conductive and significantly more noble than the substrates [12], so that the cathodic reaction occurs on the surface of the coatings and the metal dissolution on the base metal and is further intensified by the galvanic effect [16]. A low ratio of anode to cathode surface area leads to “pitting” [15] and detachment of the coating, which is mechanically stressed by the formation of a voluminous iron oxide [4].

Provided that the coating is inert and has good adhesion, the severity of corrosion of the base metal depends on the type of substrate, the degree of porosity of the coating and the corrosiveness of the environment. Based on the poor protection offered by a columnar structured TiN coating on 99.5 % iron, Elsener *et al*. [17] concluded that effective corrosion protection can only be achieved on passive substrates where the porosity of the coating is less relevant. However, by improving the barrier properties, the hard coatings were also able to provide good corrosion protection on non-passive substrates such as low-carbon steels USt 37-2 [18] and API grade X-52 [19], which are often used in construction, carbon steels such as AISI 1045 [5,20] and CK45 [6], which are mostly used in general engineering and industry, and tool steels such as AISI M2 [21] and X12 M [18], which are most frequently used in the manufacture of cutting and forming tools.

The established solutions to reduce permeable defects are to optimize the parameters of the coating process to obtain coatings with a denser morphology, to increase the thickness of the coating, to form multi-component coatings by adding elements that improve passivity and have the ability to seal pores, and to introduce a noble and dense interlayer between the coating and the substrate [4,7,8,11,22,23]. Nowadays, scientists are striving to develop sophisticated schemes to

modify the morphology and architecture of hard coatings by changing their crystallographic structure and/or applying multiple layers [18,22,24-28]. Fast, reliable, and sensitive assessment of hard coating integrity is crucial for both scientific and technological advancements, especially as the development of increasingly advanced hard coatings relies on incremental improvements driven by extensive experimentation and iterative optimization.

Electrochemical impedance spectroscopy (EIS) is a method that is particularly suited for in-depth studying the integrity of hard coatings because it captures the complexity of the substrate/hard coating/corrosive environment system by revealing its resistive and capacitive properties [14,22,28]. This study aims to develop a rapid EIS screening method specifically for *in situ* detection of hard coatings barrier performance, which has, to our knowledge, not been done before. *In situ* characteristic refers to the direct assessment of coatings on metallic substrates without requiring the cutting out the sample. This capability, along with the non-corrosive nature of EIS, opens new possibilities for evaluating coating integrity in industrial and operational environments without interfering with the functional use of the coated object. While the study focuses on electrochemically inert plasma-assisted chemical vapor deposition (PACVD) coatings on electrochemically active (low to medium alloy) steel substrates, the approach could be extended to other types of hard coating/substrate systems.

The EIS studies of hard coatings on active steel substrates are relatively rare. Additionally, some reports present parameters in incorrect units and/or outside a physically meaningful range, therefore, those parameters are not reproduced herein. It should be noted that, in general, the depth of EIS analysis varies significantly among studies of hard coatings. It is mostly assumed that the coating is inert, and the substrate is active, so the equivalent circuit R_s-CPE1‖(R_{po}-(CPE2‖(R_p)) proposed by Mansfeld [29] for electrodes covered by porous polymer coatings is appropriate [19]. R_s represents the electrolyte conductivity, the high-frequency impedance response is attributed to the capacitive (C_c) and resistive (R_{po}) behaviour of the porous coating, while the low-frequency response corresponds to the capacitive (C_{dl}) and resistive (R_p) behaviour of the exposed substrate within the pores. Studies on hard coatings typically use constant phase elements (CPEs) instead of ideal capacitances to account for deviations from purely capacitive behaviour. This leads to the equivalent circuit representation: R_s-CPE1‖(R_{po}-(CPE2‖(R_p)). The impedance of a CPE is defined as: $Z_{CPE} = 1/(Q\,(j\omega)^n)$. Here, Q / F cm^{-2}s^{n-1} is the double-layer capacitance-related parameter, and n is the dimensionless CPE exponent [30]. The system's capacitive characteristics are rarely discussed. To bridge this gap, we provide a detailed explanation of CPEs role in the discussion section. It is also worthwhile to provide a brief review of EIS equivalent circuit parameters from the literature, including those for TiN-based coatings on active steel substrates in electrolytes of varying corrosivity, as these systems closely resemble the one investigated. Such a review is currently lacking in the literature, and gaining insight into the range of impedance parameters will contribute to a more comprehensive evaluation of these coatings.

Florez *et al*. [21] investigated the electrochemical impedance behaviour of ZrN, TiN, CrN, NbN, and TaN coatings deposited on AISI M2 tool steel in 3 % NaCl solution after 7 days of immersion. The coatings were deposited using an unbalanced magnetron sputtering system, with two different geometric imbalance coefficients: KG = 1.3 and KG = 0.85. The study reports the R_{po} resistance and R_p which were highest for the ZrN (KG = 1.3) coating, of the order of 10 and 100 kΩ cm², respectively. In contrast, these parameters were lowest for the TaN (KG = 0.85) coating, both order of 1 kΩ cm². The study reported only the CPE values but did not explicitly relate CPE values to coating behaviour. The high-frequency CPE exponent ranged from 0.73 to 0.85, and the low-frequency CPE exponent

ranged from 0.51 to 0.80. The charge transfer resistance of uncoated AISI M2 steel was reported as 11 kΩ cm², significantly lower than that of ZrN (KG = 1.3), confirming the enhanced corrosion resistance provided by this coating compared to the bare substrate.

Kameneva *et al.* [18] studied DC magnetron sputtering deposited TiN, ZrN, (Ti,Zr)N, and (Ti,Zr,Al)N coatings on USt 37-2 steel in 0.3 % NaCl, 3 % NaCl and 5 % NaOH solutions. The R_p value for bare steel in 3 % NaCl was 2.4 kΩ·cm², while the best-performing coating (Ti,Zr,Al)N, achieved 62 kΩ cm² in the same environment. For the TiN-ZrN multilayer coating, R_p was 186 kΩ cm² in 0.3 % NaCl and 550 kΩ cm² in 5 % NaOH. The CPEs were not reported.

Ali *et al.* [19] investigated the corrosion resistance of TiN, TiB_2, TiBN coatings deposited by CVD on low-carbon steel (API grade X-52) in simulated soil solution (SSS: 2.5 mmol/L NaCl, 5.0 mmol/L $NaHCO_3$, 5.0 mmol/L $Na_2SO_4{\cdot}10H_2O$). After 6 hours of exposure, the R_p values were 1.55 kΩ cm² for bare steel, 5.2 kΩ cm² for the worst performing TiB_2 and 4.47 MΩ cm² for the best performing TiBN coating. The related R_{po} values were 0.1 kΩ cm² for TiB_2 and 0.747 MΩ cm² for TiBN coating. The CPEs were not reported. In another study, Ali *et al.* [10] found R_{po} equal to 10 MΩ cm² and R_p to 26.8 MΩ cm² for the exceptionally well-performing TiBN coating in SSS after 90 days of exposure. Capacitances were reported and were all the order of 1 µF cm^{-2}. The CPE exponent *n* values were 0.7-0.81 for the low frequency CPE and 0.95 for the high frequency CPE.

Landek *et al*. [24] investigated the corrosion resistance of a TiN/TiCN gradient multilayer coating deposited by PACVD on X37CrMoV5-1 hot-work tool steel in 3.5 % NaCl solution. After 30 minutes of exposure, the R_p value was 0.932 MΩ cm², while R_{po} was significantly lower, at 101 Ω cm^2. CPEs were reported but not discussed.

Elsener *et al*. [17] compared the impedance behavior of TiN coatings deposited by physical vapor deposition (PVD) and chemical vapor deposition (CVD) on various substrates, including carbon steel, in deaerated 1 M HCl solution. PVD TiN exhibited a low-frequency resistance of the order of 1 kΩ cm² on both carbon steel and stainless steel, while CVD TiN showed similar resistance on carbon steel but significantly higher values, of the order of 100 kΩ cm², on stainless steel. Resistances of 1 MΩ cm² and higher were only attained on TiAlV and quartz glass, aided by the inertness of these substrates. The low-frequency double layer capacitance values were between 180 and 280 µF/cm², while the coatings high-frequency capacitance was around 50 µF/cm².

It can be concluded from the above-mentioned references that in neutral solutions, the DC limit of resistance (R_{dc}), which is the sum R_{po} and R_p, varies between $R_{dc} \propto$ 1 kΩ cm^2 for the bare substrate and $R_{dc} \propto$10 MΩ cm^2 for excellently performing coatings [10,19]. Coatings with $R_{dc} \propto$10 kΩ·cm^2 are considered to have poor barrier performance, and the coatings with R_{dc} > 100 kΩ cm^2 are usually rated as good.

In this study, we employed a conventional measurement procedure, stabilizing the working electrode in the electrolyte while simultaneously recording the open circuit potential (OCP), followed by the acquisition of impedance spectra. However, for the first time, we utilized a press-on cell filled with a paste electrolyte. The detailed geometric design and dimensions of the paste electrolyte cell have been previously described [29,31]. A schematic representation of the cell is provided in the experimental section. The cell uses a quasi-solid-state, chloride-free, pH-neutral electrolyte, originally developed for electrochemical impedance spectroscopy applications by Bera *et al*. [31,32] and Šoić *et al*. [33], who extensively studied its properties and advantages in their previous works. The paste electrolyte cell has been successfully applied to characterize the protective patina and polymer coating layers on bronze [33], oxide layers and effectiveness of passivation treatments on welded stainless steel [31], as well as assessing the protective properties of a naturally formed 44-year-old patina and the efficiency of artificial patination on weathering steel [32].

Building on these findings, we hypothesize that the method, using a paste electrolyte with negligible corrosivity, would enable non-destructive electrochemical characterization of the barrier effect of hard coatings and differentiation of the hard coatings across the entire spectrum of barrier effect. To verify the hypothesis, the four coating/substrate combinations involving TiN/TiCN and TiN/TiBN bilayers on 42CrMo4 and 32CrMoV12-10 were characterized by EIS, and in parallel, by quantitative glow-discharge optical emission (GD-OES) elemental profiling [10,34-36]. Scanning electron microscopy (SEM) image analysis [2,37-41] was utilized to quantify variations in surface morphology among the samples as an independent method to substantiate EIS observations. Mirror-finish platinum foil and CR4 cold-rolled steel were used as reference samples at opposite ends of the corrosion susceptibility spectrum, serving as an additional means of method validation. Additionally, a thorough literature analysis was conducted to extract numerical EIS data from studies on similar hard coating/substrate systems in neutral liquid electrolytes, which were then incorporated into the discussion for validation and comparison.

Experimental

Two types of substrates, 42CrMo4 and 32CrMoV12-10, labelled with the letters A and B, respectively, were PACVD coated with two types of multilayer coatings consisting of multiple TiN/TiBN and TiN/TiCN bilayers, labelled with numbers 1 and 2, respectively, resulting in four different combinations of substrates and coatings: A1, B1, A2 and B2. The chemical composition of the steel substrates, both nominal (from standards) and as measured by GD-OES, is presented in Table 1.

Table 1. *Nominal and GD-OES measured chemical compositions of the steel substrates used in the study. Nominal values are based on standard specifications, while measured values were obtained via glow discharge optical emission spectroscopy (GD-OES)*

	Content, wt.%							
	C	Mn	Si	P	S	Cr	Mo	V
42CrMo4 (A) from EN ISO 683-2	0.38-0.45	0.60-0.90	0.10-0.40	0.025 max	0.035 max	0.90-1.20	0.15-0.30	-
Measured	0.42	0.67	0.24	0.011	0.005	1.05	0.23	-
32CrMoV12-10 (B) from EN 10085	0.30-0.35	0.40-0.60	0.20-0.35	0.015 max	0.001 max	2.80-3.30	0.80-1.20	0.25-0.35
Measured	0.32	0.46	0.29	0.019	0.001	2.93	0.85	0.26

The PACVD process was used for the coating under a pressure of 200 Pa (2 mbar) and a temperature of 520 °C in an atmosphere consisting of the process gases Ar, N_2, H_2, BCl_3, CH_4 and $TiCl_4$ vapor in various combinations and flow rates. In the steps preceding deposition, the samples were polished, degreased, heated, plasma cleaned and finally plasma nitrided to reduce the hardness gradient between substrate and coating [42]. Polishing was performed successively using SiC abrasive papers with grit sizes 600, 800 and 1200, followed by alumina (Al_2O_3) suspensions with particle sizes of 1.0, 0.3 and 0.05 µm, applied in that order. The coatings were applied in cycles to form a gradient layer consisting of 16 bilayers with TiN on the bottom and TiBN or TiCN on top.

Quantitative GD-OES element profile measurements were performed using a Leco GDS-850A spectrometer with a Grimm excitation source in DC mode suitable for conductive samples. The surface area tested was 12.5 mm^2.

The morphology of the coatings was examined using secondary electron scanning electron microscopy (SE-SEM). The SE-SEM analysis was performed using a VEGA 3 SEM (TESCAN) at an accelerating voltage of 10 kV and a working distance of 22.85 mm. Images were acquired at three different imaging scales, corresponding to scale bars of 20 µm, 5 µm, and 2 µm. The SE-SEM images were analysed using the free, open-source software ImageJ [38,43].

The open circuit potential and EIS measurements were performed using the ReCorr® QCQ device and the paste electrolyte cell previously described in detail in references by Bera *et al*. [31,32]. The experimental setup is presented in Figure 1. In brief, the cell consists of a non-conductive rubber block with a shallow cylindrical cavity, 5 mm deep and 1.7 mm in diameter. The bottom of the cavity is formed by the hard-coated surface, which serves as the working electrode, with an exposed area of 2.69 cm^2. A fixed volume of around 1.13 cm^3 of paste electrolyte is applied into the cavity. The cell lid is a circular conductive rubber counter electrode with a cylindrical stainless steel quasi-reference electrode (6 mm in diameter) embedded at its centre. A consistent 5 mm separation is maintained between the working electrode on one side and the counter and reference electrodes on the other side.

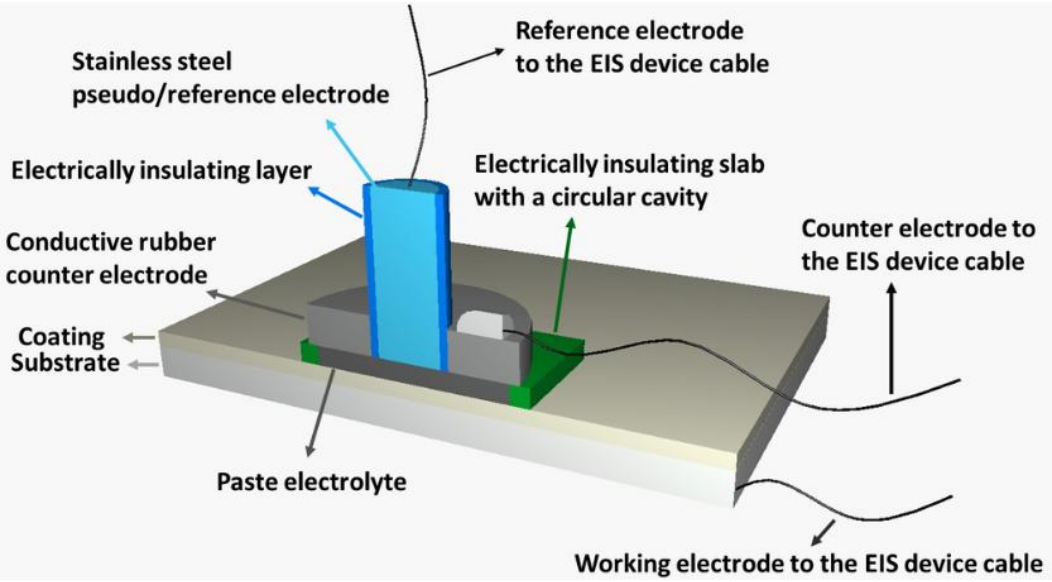

Figure 1. *Schematic cross-section representation of the paste electrolyte electrochemical cell in the fully assembled state*

The paste electrolyte is an ionic conductor, formulated as a conductive paste that consists of a water-based electrolyte phase combined with natural wax, glycerol, and carbon black to optimize conductivity and adhesion. The term quasi-solid-state describes its intermediate nature between a liquid and a solid, while it retains the ability to facilitate ion transport like a liquid, its viscosity and structural integrity prevent free flow and spillage, ensuring a stable electrode interface. This stability means that the electrolyte remains in place during measurement and maintains a constant electrode area, providing conditions conducive to reproducible electrochemical data. The pH-neutral nature and the absence of chloride ions further reduce the risk of significant corrosion during EIS measurements, as demonstrated in studies on bronze and stainless steel substrates [31,33].

The potential of the QCQ pseudo-reference electrode is sufficiently stable compared to the saturated calomel electrode (SCE) in the electrolyte paste and equals 60±8 mV [32]. All OCPs measured in this study were recalculated to SCE using a 60 mV offset. All OCP and EIS measurements were performed in triplicate at three different positions on each coated sample. The sample dimensions were 50×20×10 mm. For comparison, the measurements were performed on a mirror-finish platinum (Pt) foil and a cold-rolled (CR4) steel plate purchased from C&W Specialist Equipment, United Kingdom, which was abraded with 600 grit sandpaper. All samples were degreased in ethanol using an ultrasound bath for five minutes and dried with a nitrogen stream immediately before measurement. On all samples, the OCP was recorded every second for 1000 s before the EIS spectrum measurement. EIS spectra recording at the OCP in a frequency range of 10^5

to 10^{-2} Hz, and the AC signal amplitude of 10 mV took around six minutes. The fitting of equivalent circuits to impedance spectra was performed using PCTrace software (PalmSens, The Netherlands).

Results and discussion

GD-OES profiling of coatings

Figures 2a to d show GD-OES depth profiles of Fe, Ti, N, C and B for samples A1, B1, A2 and B2, respectively. The samples were coded using the following scheme: substrate A corresponds to 42CrMo4, substrate B to 32CrMoV12-10, coating 1 represents TiN/TiBN, and coating 2 represents TiN/TiCN. All the profiles show a zone where the Ti and N concentrations decrease, and the Fe concentration increases with depth until the substrate is reached.

The high carbon signal contained on the surface probably comes from the contamination of the surface [36]. The sharp decrease in the carbon content at the surface for TiN/TiBN coating corresponds to the increase in the Ti and N content. In the case of the TiN/TiCN coating, a significant carbon content remains present in the coating.

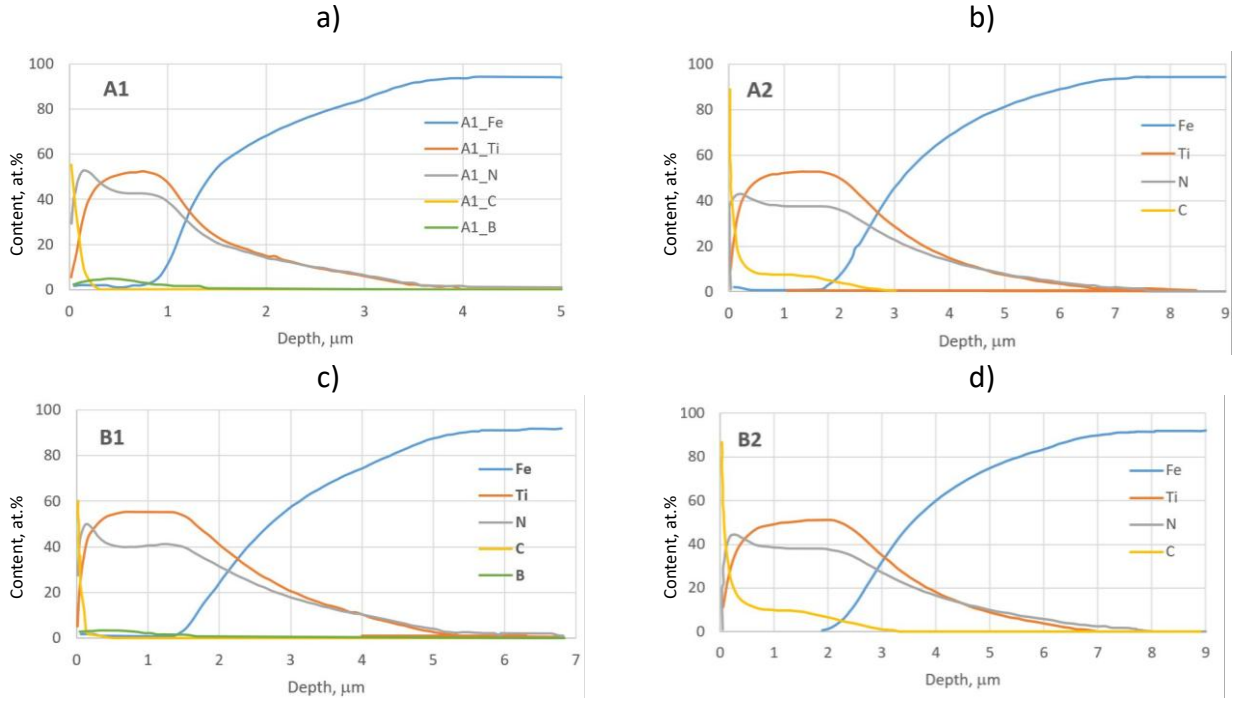

Figure 2. *Quantitative GD-OES element depth profiles of the multilayer coatings deposited on different steel substrates. The profiles reveal graded interfaces, characterized by decreasing Ti and N signals and increasing Fe content with depth, which confirms a smooth transition from coating to substrate - a typical feature of PACVD processes*

The Ti and N elements in the coating are present as titanium nitride, but the ratio Ti/N determines the character of the bonds [34], which are more metallic at high Ti/N ratios and more covalent at low Ti/N ratios. In all samples, nitrogen enrichment is present at the surface. The Ti/N ratio calculated from the GD-OES data decreases at the surface [35], reaching a minimum of about 0.15 and 0.25 for samples A1 and B1, respectively, and 0.5 for samples A2 and B2. More covalent bonds in the nitrogen-enriched layer and a high electron density shielding the underlying Ti atoms [6] probably improve the electrochemical stability of the TiN/TiBN (A1 and B1) coating material. The smooth transition between the coating and the substrate indicates that the coatings have a graded composition rather than a sharp boundary with the substrate [44]. The width of the transition zone is about 4 µm for A1 and B1 coatings and about 7 µm for A2 and B2 coatings.

Scanning electron microscopy image analysis

The SE-SEM images of the samples are shown in Figure 3. To ensure comparability [37], only the imaging scale was varied (as indicated by the scale bars), while the accelerating voltage (10 kV) and working distance (22.85 mm) were kept constant.

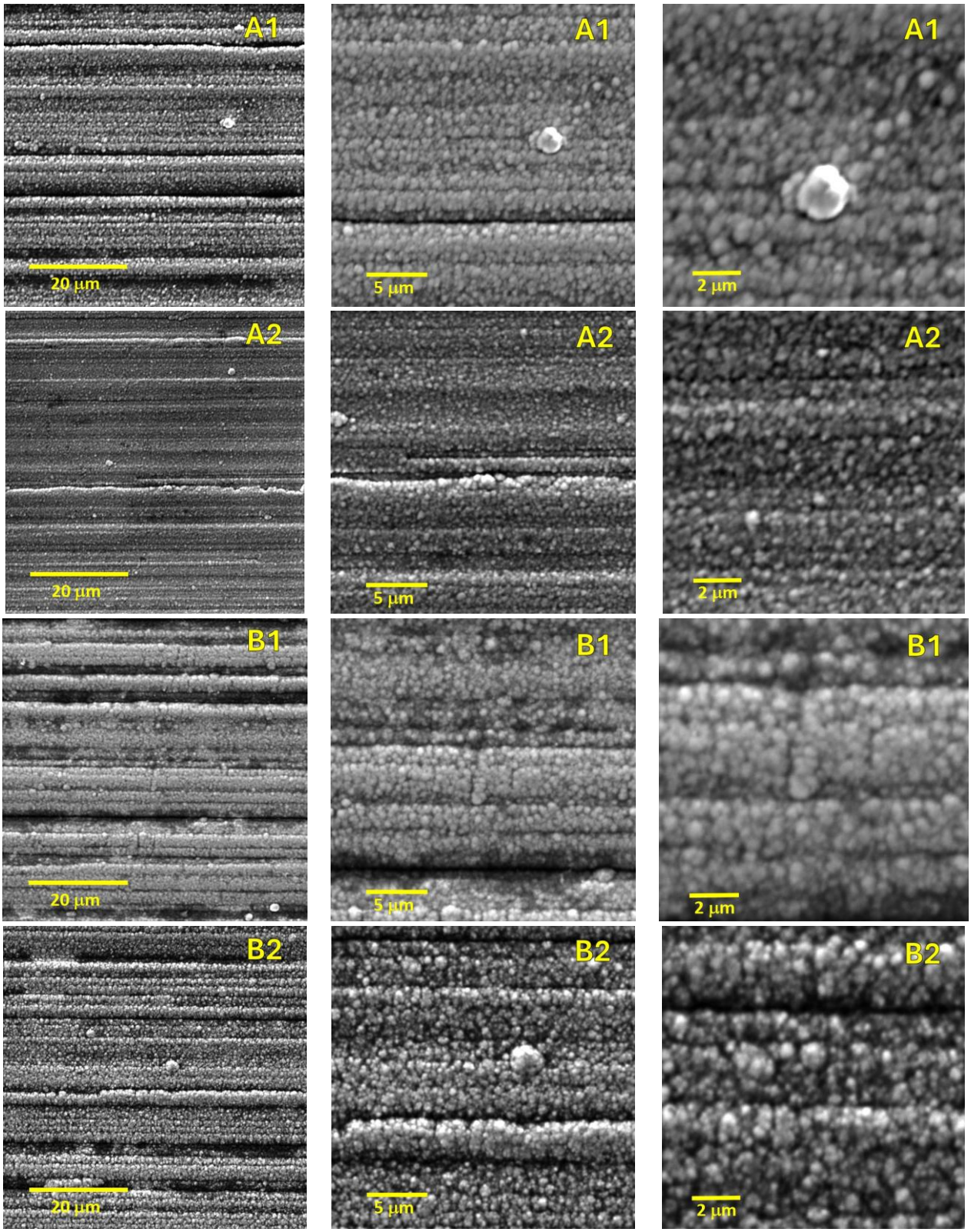

Figure 3. *Secondary electron SEM (SE-SEM) images of the coating surfaces acquired at three imaging scales (as indicated by scale bars) show the surface morphology and microstructural features of the TiN-based multilayer coatings. Differences in brightness and surface texture reflect variations in roughness and grain boundary density between coating types and substrates*

The images reveal a grainy surface with a striated pattern, most prominently observed at the lowest imaging scale (as indicated by the 2 µm scale bar). At higher imaging resolution, the individual grains exhibit a domed appearance and are separated by distinct grain boundaries, which is characteristic of PACVD coatings [45]. The density of these grain boundaries can influence the barrier properties, either enhancing or reducing the coating's effectiveness. In monolayer coatings, an increased number of grain interfaces can be achieved by changing the structure from columnar to equiaxed, and/or by reducing the grain size to create denser coatings, which act as better barriers. For example, CrAlN and CrN coatings are characterized by epitaxial microstructures [22], which do not provide direct diffusion paths for corrosive solutions and exhibit higher passivity than TiN coatings due to the stronger passivation ability of Cr [7]. By adding boron to the TiN layer, a coating with competing TiN and TiB_2 phases is obtained [10,11,25]. Crystal refinement and higher coating density are achieved because TiB_2 has a uniformly distributed fine-grain morphology, resulting in TiBN coatings with a multi-oriented structure. Ultrafine-grained coatings have been shown to be excellent diffusion barriers for medical applications [26]. Multi-layer coatings have proven to be even more resistant to corrosion than single-layer coatings. This is due to the increased number of interfaces caused by finer grain sizes and interruptions in crystallographic alignment between the layers. The resulting disordered microstructure provides fewer opportunities for the electrolyte to reach the substrate through cross-layer continuous paths [5]. The fine-tuning of multilayer coatings, which has a significant impact on their properties, involves adjusting the thickness of the layers, the number of interfaces and the properties of the interfaces [27].

However, the opposite role of grain size in reducing corrosion resistance is also reported in the literature. This is attributed to the increased grain boundary density in fine-grained coatings, which may enhance the number of paths for the transport of corrosive solutions to the substrate, especially when the coating surface lacks pronounced passivity [7,21].

To characterize the grain boundaries of the investigated samples, the SE-SEM images, originating from the electron beam reflected from the top 1 to 30 nm of the sample surface [38], are particularly well-suited, as the electron beam is highly sensitive to surface topography [40]. In Figure 3, the SE-SEM images show that grain surfaces more exposed to the electron beam appear brighter, while grain boundaries, shielded from the beam, appear darker. Based on this observation, image analysis could provide an objective method for ranking SEM images by grain boundary density. When combined with EIS data, this approach could offer insights into the role of grain boundaries in the barrier effect of the investigated coatings.

To our knowledge, there is only one reference, that of Perumal *et al.* [46], which explicitly correlates hard coating SEM image analysis with EIS. Surface roughness and coating defects are two dominant factors which were assumed to affect corrosion of the investigated TiN coatings with an average thickness of 3 µm applied using cathodic arc deposition on stainless steel and exposed in 3.5 % NaCl. Surface roughness was primarily analysed using first-order statistical features, mean, standard deviation, and entropy and second-order statistical features, contrast, homogeneity, and energy, which were found appropriate to describe the texture of the coating surface that has a stochastic nature. Coating defects were identified and quantified using binarization technique with the binarization threshold set at 50 % of the average mean grey level intensity of the grayscale image. The defect density was calculated by summing the defective pixel areas and dividing by the total image area. A strong linear correlation was found between defect density (calculated from binarized SEM images) and the porosity of the coatings. A multiple linear regression model showed that the following contrasts, homogeneity, entropy and standard deviation of the greyscale had significant linear relationships with the corrosion rate.

In the present study, we utilized first-order statistical image features [39,46], including grayscale mean, standard deviation, kurtosis, and skewness, to analyse the surface morphology of the coatings. These features were used to quantify the intensity distribution within the images, indirectly reflecting morphological characteristics defined by the specimen features and grain boundaries. To achieve this, we analysed 8-bit SEM images of the coating surfaces acquired at three imaging scales, corresponding to image areas of 3995.4, 655.4, and 163.8 μm². These scales are referred to throughout as 20 μm, 5 μm, and 2 μm, based on the scale bars shown in the images.

The histograms, which show the number of pixels as a function of grayscale intensity ranging from 0 (black) to 255 (white), are shown in Figure 4. The analysis was performed on entire image areas of 3995.4, 655.4, and 163.8 μm², corresponding to the largest, intermediate, and smallest imaging scales used. The analysis of smaller but representative areas did not yield significantly different results, so the entire image was considered representative. The only exclusion was the white spot visible in the highest-resolution image of the A1 sample. It was cut out of the image and not included in the analysis.

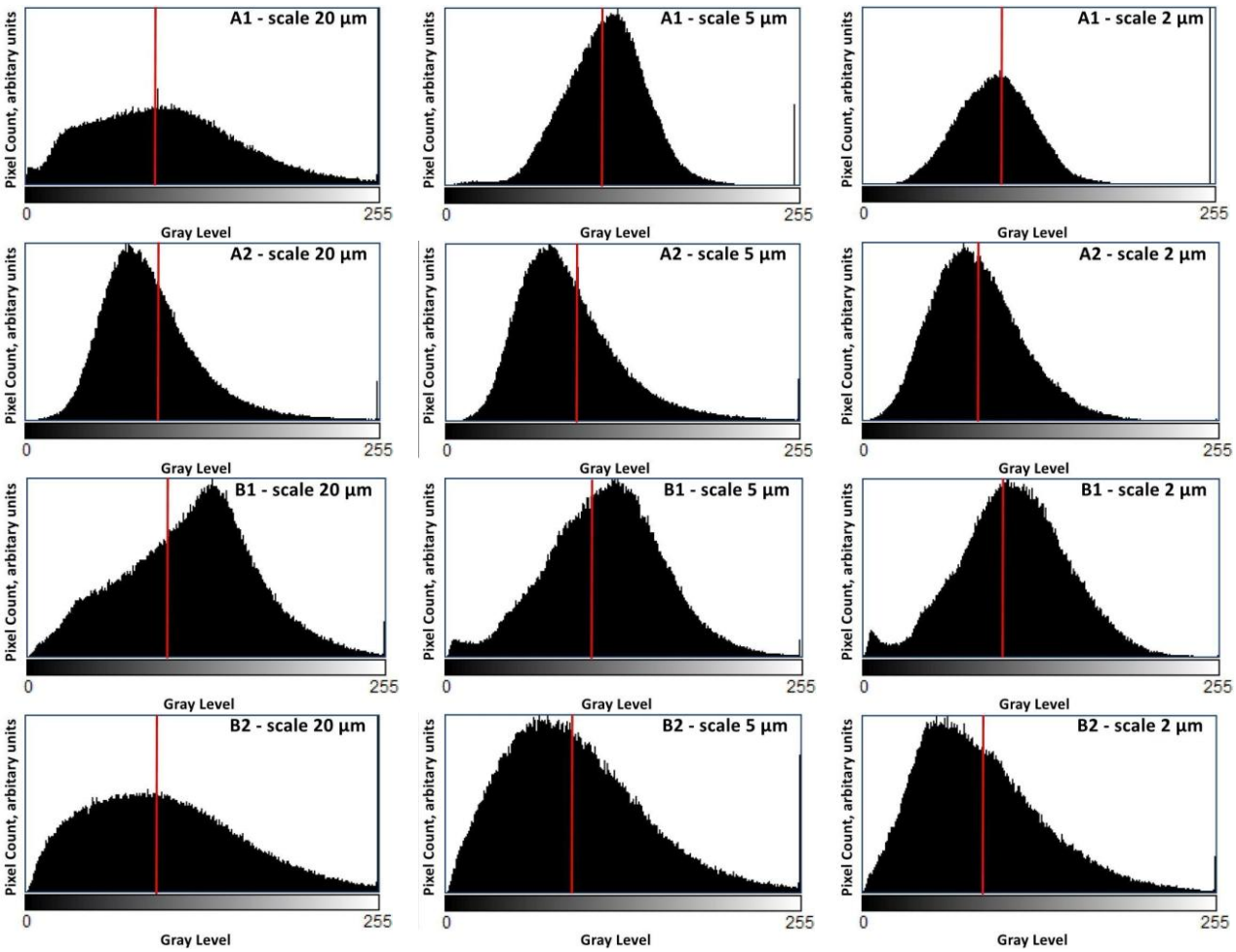

Figure 4. *Grayscale histograms of the SE-SEM images for each sample, representing the distribution of pixel intensities across three imaging scales. The red line indicates the binarization threshold determined using Li's method [47], which minimizes the cross-entropy between the original and binarized image*

The histograms appear unimodal, apart from some enlargements of the A1 and B1 samples, which show bimodal histograms with two more or less clearly recognizable peaks. The two distinct peaks are slightly visible at the largest imaging scale (20 μm). The red lines denote thresholds for image binarization determined using Li's method [47], which is introduced in detail later in the text.

Quantitative descriptors of the histograms, the mean, the standard deviation (square root of variance), the skewness and the kurtosis were calculated for the original SE-SEM images shown in Figure 3. The averaged histogram parameters across all imaging scales are shown in Figure 5, with standard deviations represented as error bars to indicate data dispersion. These findings directly reflect the morphological characteristics of the coatings.

The ranking of greyscale mean is B1>A1>B2>A2. The greyscale means of the samples A1 and B1 (TiN/TiBN coating) shown in Figure 5a is 15 and 20 % higher, respectively, than that of samples A2 and B2 (TiN/TiCN coating), indicating that A1 and B1 have brighter images which is a likely indication of more reflective coatings, with less dense grain boundaries. The ranking of greyscale standard deviation is B2>B1>A2>A1. The standard deviation is higher for samples B1 and B2 (32CrMoV12-10 substrate) and lower for samples A1 and A2 (42CrMo4 substrate), showing that the images of samples A1 and A2 have a wider distribution of grayscale intensities suggesting higher surface heterogeneity of the coatings on 42CrMo4 substrate, which could indicate defects or weak points [39].

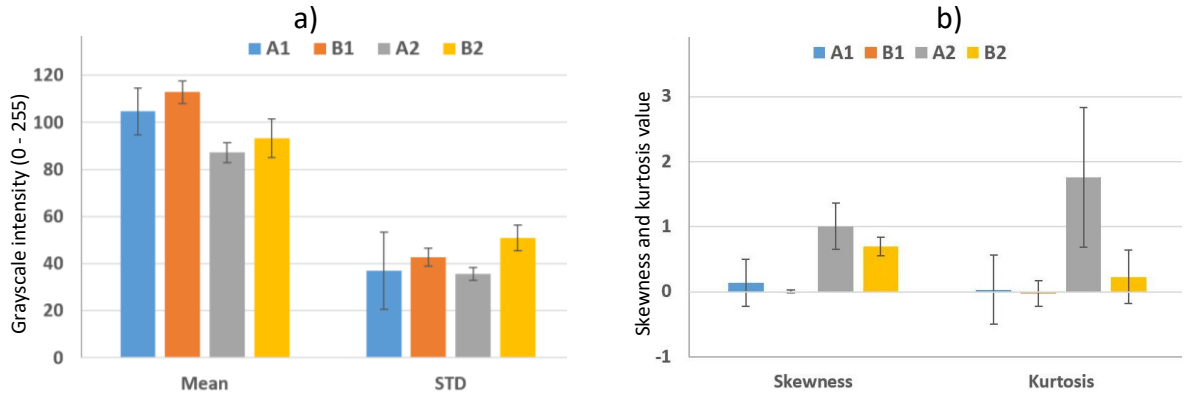

Figure 5. *First-order statistical parameters derived from grayscale histograms of SE-SEM images for each sample across three imaging scales. a) grayscale mean and standard deviation reflecting the overall brightness and contrast of the surface; b) histogram skewness and kurtosis quantifying asymmetry and peak sharpness in the intensity distribution, respectively*

Skewness and kurtosis are shown on the same dimensionless scale in Figure 5b. The skewness measures the asymmetry of the histograms. A positive value of skewness describes a histogram with an asymmetric tail that extends toward the positive, white end of the grayscale intensity, and a negative skewness has a histogram tail that extends toward the negative, black end of the grayscale intensity [39]. Kurtosis is used to quantitatively compare the histogram to a normal distribution. High kurtosis indicates a sharp histogram with more extreme values, and a low kurtosis indicates a flat histogram with fewer extreme values. The order of skewness and kurtosis is B1<A1< B2<A2, with the skewness and kurtosis of the B1 sample always very close to zero, those of the A1 sample fluctuating around zero and those of the A2 and B2 samples mostly or always positive and clearly deviating from zero. The images of the more organized grains in samples A1 and B1 (TiN/TiBN coating) exhibit more uniform grey levels. This uniformity in histograms (Figure 4) are closer to a normal distribution, with skewness and kurtosis values approaching zero. The darker regions between grains in the less organized structures of A2 and B2 samples (TiN/TiCN coating), may be interpreted through a higher grain boundary density. These boundaries cause the histograms in Figure 4 to peak toward the left side of the intensity spectrum, exhibiting positive skewness and high kurtosis, as the grain boundaries dominate the darker intensity range.

It can be concluded that the first-order histogram parameters, greyscale mean, kurtosis and skewness, differ consistently between the two coating types (1 and 2), with coating TiN/TiBN

coating (1) having a higher proportion of bright pixels. Additionally, the standard deviation of greyscale mean differentiates between the substrate types (A and B), with substrate A (42CrMo4) producing coatings with more heterogeneous grayscale distributions.

From this analysis, the B1 sample stands out as distinct, with the highest greyscale mean and skewness and kurtosis near zero (Figure 5). These values reflect a uniform intensity distribution, corresponding to a well-organized morphology and grain structure with the lowest grain boundary density. Notably, no significant negative skewness, which could indicate image charging [39], was observed in this study.

While first-order statistical features, derived from histograms, effectively describe the intensity distribution of an image, they lack spatial information about the relative positions of different grey levels within the image. These features cannot distinguish whether low grey level values are clustered together or interspersed with high grey level values, as the spatial context of each pixel is lost in the histogram analysis [39,46]. This limitation underscores the need for binarization to quantify grain boundaries versus grains by providing spatially resolved information about the coating morphology. Therefore, the image was binarized into black and white areas using Li's method [47], (Figure 6) and used to identify the percentage of bright regions (grains) and black regions (grain boundaries) in SE-SEM images from Figure 3. If a clear minimum can be found in the bimodal histogram [37], the corresponding grayscale intensity can be used as the binarization threshold. However, the threshold is often not so clearly defined for SE-SEM images as in the present case. The Li method, which minimizes the cross-entropy between the original and binarized image, was selected for its robustness in handling highly unbalanced histograms, where traditional thresholding approaches based on bimodal assumptions may fail [47].

As previously mentioned, the binarization thresholds obtained with Li's method are shown as red lines in Figure 4. The goal of binarization is to use a grayscale intensity threshold to separate the image into foreground and background objects [47], in this case, grains and grain boundaries. The regions of grains were quantified for each image based on the percentage of white area (first column in Table 2). The percentage of white area varies with imaging scale, showing a general increase for sample A2 and a decrease for samples A1, B1, and B2. This trend may be attributed to the improved resolution of finer surface features, such as grains or grain boundaries, at higher imaging resolutions, which influences the binarization outcome. Average values across all imaging scales were also calculated. The ranking of the average percentage of white area (grains) is B1>A1>B2>A2, or equivalently, of the black area (grain boundaries) is B1<A1<B2<A2.

In some binarization methods, the grayscale image must be enhanced by a series of preprocessing steps such as equalization or filtering. Li's algorithm relies on global statistics of the histogram and reportedly does not require image enhancement [47]. To test the robustness of Li's binarization under varying contrast conditions and to ensure consistent thresholding across images with differing brightness or histogram shapes, normalization and histogram equalization were applied, both separately and in combination, using 1 and 5 % normalization [43] prior to thresholding. During equalization, the intensity values are redistributed to cover the entire range from 0 to 255, which increases the contrast of the image. On the other hand, normalization causes 1 % and 5 % of the darkest and brightest pixels to be considered black and white, respectively. The rest of the image intensities are stretched to fit into the respective 1 to 99 and 5 to 95 % range, making the image more balanced. The contribution of the white area was calculated separately for all images in Figure 6, both in non-equalized and equalized states (E), without normalization (N0) and normalized

at two levels: N1 (1 % share) and N5 (5 % share). Average values across all imaging scales were also calculated, and the results are presented in Table 2.

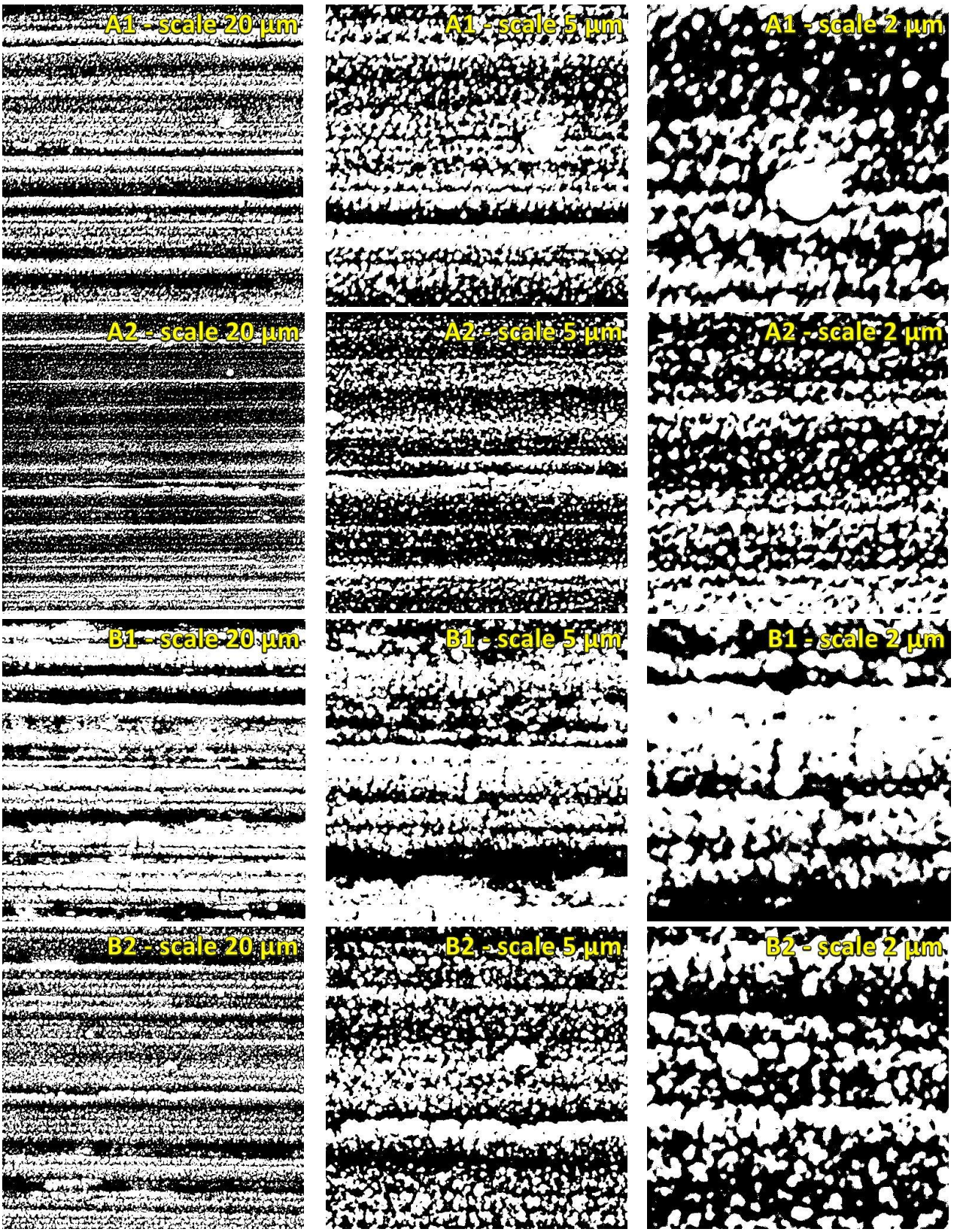

Figure 6. *Binarized SE-SEM images for each sample at three imaging scales, processed using Li's thresholding method [47] applied to the corresponding grayscale histograms. The binarized images highlight grain boundaries and surface features with high contrast, allowing quantification of boundary density and morphological complexity*

Table 2. *Contribution of the white area on the coating surfaces in SE-SEM images binarized using Li's method, shown across different imaging scales and preprocessing conditions: normalization (N) and histogram equalization (E)*

Samples – imaging scale	*Contribution of the white area, %*					
	N0	N1	N5	E N0	E N1	E N5
A1 – scale 20 μm	53.8	55.2	56.5	57.9	57.9	59.9
A1 – scale 5 μm	57.1	61.0	64.8	59.7	59.7	62.2
A1 – scale 2 μm	45.0	46.3	56.2	57.6	58.9	60.3
Average	**51.9**	**54.1**	**59.2**	**58.4**	**58.8**	**60.8**
B1 – scale 20 μm	65.8	67.1	69.6	63.1	63.8	64.5
B1 – scale 5 μm	60.1	61.9	64.6	61.0	61.0	61.9
B1 – scale 2 μm	58.6	59.6	61.7	58.6	58.6	61.7
Average	**61.5**	**62.9**	**65.3**	**60.9**	**61.1**	**62.7**
A2 – scale 20 μm	37.7	41.1	46.0	53.8	53.8	56.5
A2 – scale 5 μm	38.2	41.4	44.8	53.3	53.3	55.9
A2 – scale 2 μm	47.0	49.3	53.1	56.9	56.9	58.2
Average	**41.0**	**44.0**	**48.0**	**54.7**	**54.7**	**56.9**
B2 – scale 20 μm	51.4	52.8	54.1	56.8	58.1	58.8
B2 – scale 5 μm	51.4	48.8	51.2	56.8	56.8	57.6
B2 – scale 2 μm	44.6	45.4	48.7	54.9	55.8	56.6
Average	**49.2**	**49.0**	**51.3**	**56.2**	**56.9**	**57.7**

The average percentage of white area always increases with the introduction of normalization and the increase of the normalization percentage due to the progressive loss of image details caused by the binarization of the distribution ends. The percentage of white area increases even more significantly with equalization. These results show that image properties are sensitive to image enhancement. Nevertheless, the ranking of the average white and black area percentages remained the same.

To conclude, the ranking of samples deduced from first-order statistical features of SEM images and from binarization analysis is consistent, both indicating the relative density of grain boundaries of the samples. Additionally, the standard deviation of the greyscale indicates the difference in homogeneity of the coatings obtained on different substrates.

Electrochemical impedance spectroscopy results and analysis

Open circuit potential (OCP) stabilization preceded EIS measurements. The OCP of the coated samples as a function of time is shown in Figure 7.

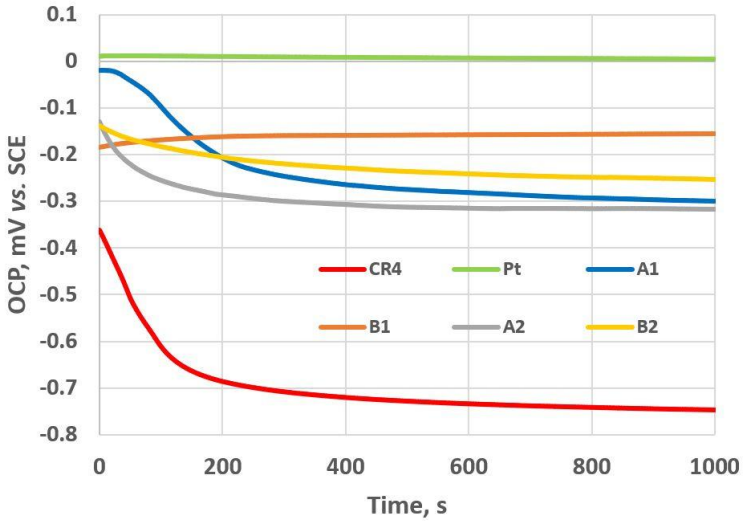

Figure 7. *Open circuit potential (OCP) stabilization over 1000 seconds for the uncoated reference materials (CR4 and Pt) and for the coated samples (A1-B2). OCP was recorded prior to electrochemical impedance spectroscopy to assess surface stability in the test environment*

A stabilization period of 1000 s was chosen as a compromise between measurement speed and system stabilization. This timeframe aligns with established practice in studies on similar titanium-based ceramic coatings, where a 15-minute OCP stabilization was routinely used before EIS measurements [10,19]. It can be observed that OCP effectively differentiates between the coatings. Additionally, the OCP was recorded for platinum, which was chosen as a representative noble metal surface and for cold-rolled CR4 steel, which was selected as a representative active metal surface. The measured OCP values for the hard-coated samples lie between those of CR4 steel and Pt.

If the coatings themselves are to be compared, it should be noted that the OCP depends not only on the exposed substrate area but also on the type of coating, substrate, and local conditions within the pores [10]. Due to the mixed potential arising from galvanic coupling between the coating and the substrate [12], OCP is not a strictly reliable indicator of coating integrity but may serve only as a tentative indicator, where more positive OCPs denote dense and protective coatings, whereas less positive OCPs suggest porous coatings [4,25]. Direct comparison of OCPs across different systems, particularly those with distinctive coating/substrate/electrolyte combinations, is therefore not straightforward.

Table 3 is based on an extensive literature survey, compiling OCP values and the impedance DC limit (R_{dc}), calculated as the sum of high-frequency (R_{po}) and low-frequency (R_p) resistances, for TiN-based coatings on low- to medium-alloy steels exposed to neutral liquid electrolytes. The measured OCP values in this study show strong agreement with the literature data, supporting the validity of the proposed method despite variations in electrolyte composition, system conditions, and stabilization times.

Table 3. *OCP and total resistance (R_{dc}) values of TiN-based hard coatings on unalloyed and low-alloy steels in neutral and acid electrolytes from the literature (OCP from the references was converted to the SCE reference electrode scale)*

Substrate	Coating	Stabilization time / solution	OCP, mV vs. SCE	R_{dc} / kΩ cm^2	Ref.
Low-carbon steel	-	2 days / simulated soil solution	-744	-	[10]
	TiBN-3		-360	20200	
	-	2 days / simulated seawater	-813	-	
	TiBN-3		-323	>>10^4	
Low-carbon steel	PVD TiN	1 M HCl	-390	9.8	[17]
	CVD TiN		-445	6.9	
USt 37-2 steel	-	until stabilized / 3 % NaCl	-661	2.4	[18]
	TiN	until stabilized / 0.3 % NaCl	-380	150	
Low-carbon steel	-	6 h / simulated soil solution	-649	1.36	[19]
	TiN		-429	17.76	
	TiB_2		-620	5.2	
	TiBN-1		-192	122.7	
	TiBN-2		-13	4469.2	
AISI M2 tool steel	-	7 days / 3 % NaCl	-657	11	[21]
	TiN		-559	17.5	
	TiN		-585	12.92	
X37CrMoV5-1 hot-work tool steel	TiN/TiCN	30 minutes / 3 % NaCl	-24	932	[24]

Apart from the values of OCP, the trends in OCP over time are equally significant. Ali *et al*. [10] investigated the open circuit potential (OCP) behaviour of titanium-based ceramic coatings, including TiN, TiB_2, and TiBN (with varying boron content), applied to low-carbon and stainless steel in simulated soil solution and simulated seawater. For TiBN coatings on low-carbon steel, a positive shift in OCP over time was observed. In contrast, coatings such as TiB_2 exhibited a negative OCP

temporal trend, reflecting higher porosity and greater susceptibility to electrolyte penetration, which ultimately resulted in reduced corrosion resistance. These findings confirm that an upward OCP trend over time serves as a strong indicator of superior performance, whereas a downward trend suggests higher porosity and reduced protection. In Figure 7, CR4 sample and coated samples A1, A2, and B2 exhibit a downward trend, ultimately reaching OCP values at 1000 s between -284 and -302 mV *vs.* SCE. In contrast, Pt foil and coating B1 show an upward trend in OCP over time and B1 achieves the most positive OCP value at 1000 s of -154 mV *vs.* SCE among the coatings analysed, which indicates its superior barrier performance.

Figure 8 shows the Bode (Figure 8a) and Nyquist (Figure 8b) plots of the Pt and CR4 reference samples, and the Bode (Figure 8c) and Nyquist (Figure 8d) plots of the coated samples. The electric equivalent circuit (EEC) used, and the parameters derived for the coatings from the EIS measurements are listed in Table 4. All measurements were performed in triplicate at three different locations on the sample and the values in Table 4 are the average values. The chi-squared (χ^2) value of the order of 10^{-4} and lower was obtained for all spectra and indicated a good fit [48].

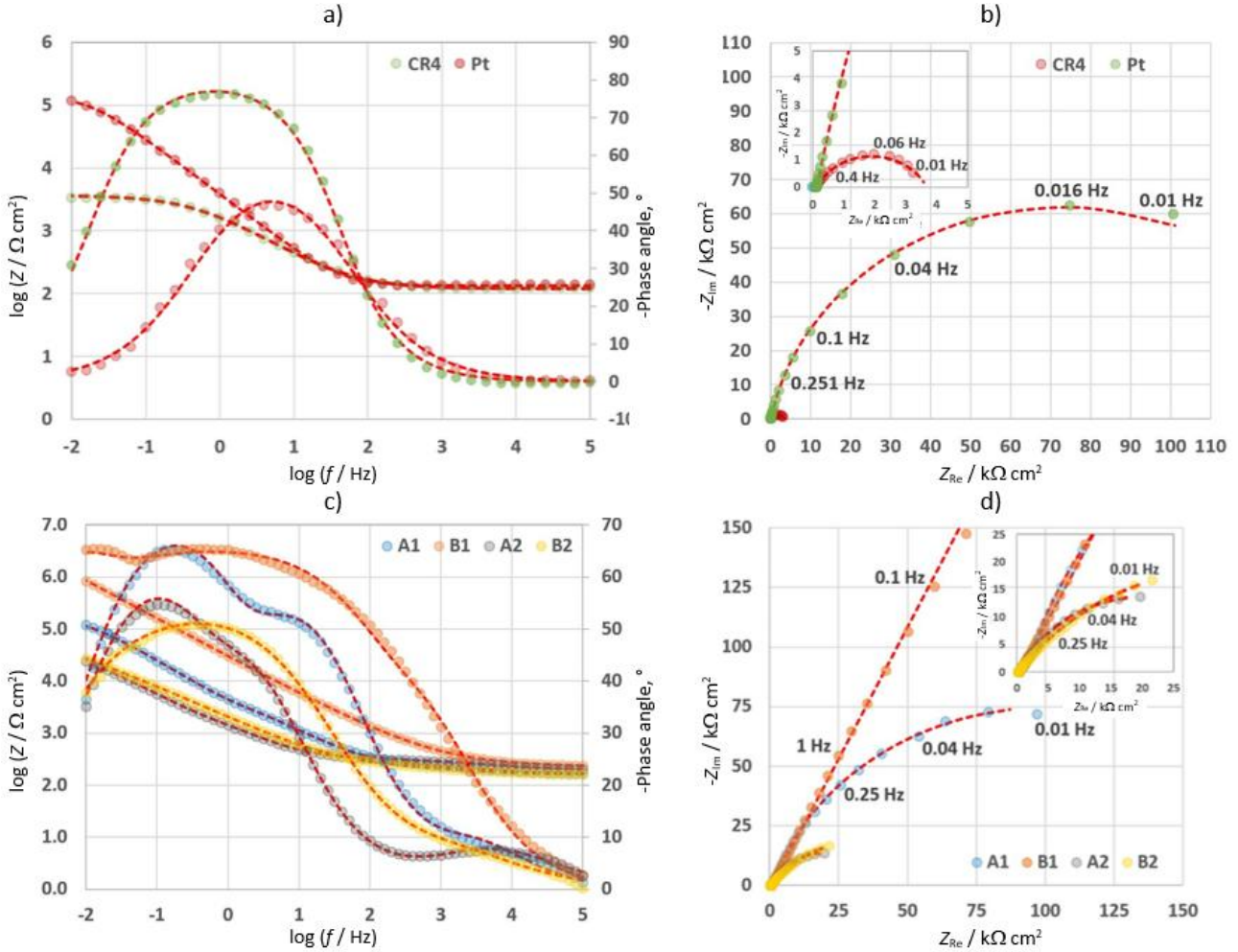

Figure 8. *Electrochemical impedance spectroscopy (EIS) results presented as Bode (a, c) and Nyquist (b, d) plots. (a, b) reference samples (Pt and uncoated CR4 steel), showing typical behaviour of inert and active metallic surfaces; (c, d) coated samples (A1-B2), demonstrating the influence of coating type and substrate on impedance response. Higher impedance magnitudes and larger Nyquist semicircles indicate superior barrier performance*

The CPE-modified equivalent circuit representing a metal coated with porous films, as described in the introduction, is identical to that used by many other authors [19] in studies of hard coatings.

Q_1 and Q_2 are the high- and low-frequency CPE parameters, as defined in the Introduction. The DC impedance limit (R_{dc}) was calculated as the sum of R_{po} and R_p, as presented in Table 3. It should be noted that the values of R_{dc} represent the extrapolated DC resistance derived from equivalent circuit modelling and not direct impedance measurements below 10 mHz. This is a standard approach in EIS analysis of porous-coated metal systems, where at the DC frequency limit, all capacitive elements cease to conduct, and the current flows solely through the resistive elements. Similar modelling and interpretation approaches can be found in prior works on TiBN and TiN coatings using porous film models [10,19].

Table 4. *Electrochemical impedance parameters derived from EIS measurements using the paste electrolyte cell*

Sample	$Z_{0.01\ Hz}$ / kΩ cm^2	Q_1 / µF cm^{-2}s^{n-1}	n_1	Q_2 / µF cm^{-2}s^{n-1}	n_2	R_{po} / kΩ cm^2	R_p / kΩ cm^2	R_{dc} / kΩ cm^2
Pt	116.5	-	-	135.8	0.893	-	159.43	159.43
C4	4.01	-	-	110.91	0.501	-	3.31	3.31
A1	152.87	5.1	0.808	12.0	0.500	127.95	171.37	299.32
B1	728.45	3.2	0.910	8.4	0.694	13882	56.37	13938
A2	23.84	85	0.792	560	0.578	34.10	2.47	36.57
B2	83.94	57	0.833	290	0.649	30.13	49.46	79.59

Although high-frequency phase angle shoulders are observed in some Bode plots (most prominent for A2 in Figure 8c), they were characterized by low resistance and proved not relevant to the primary indicator of coating barrier performance, R_{dc}. These high-frequency features were included in the equivalent circuit fits to ensure accurate modelling. However, their associated parameters were neither reported nor discussed to maintain the clarity and focus of the study.

In the present study, the electrolyte paste resistance (R) was found to be 164.33 ± 10.57 Ω cm², which is sufficiently low to allow accurate measurements on both bare and coated substrates.

Looking at the reference bare metal samples, only one semicircle is observed for these electrodes, as they lack a coating. C_{dl} could be calculated through the expression $C_{dl} = 1/(Q_2^{1/n}R_p^{(1-n)/n})$ [30]. The C_{dl} of the mirror-finish Pt foil (67.01 µF cm^{-2}) closely matches the value reported by Norlin *et al.* [50] for Pt with a smooth surface in aerated phosphate-buffered saline (60 µF cm^{-2}). Similarly, the total resistance (159.43 kΩ cm²) is comparable to Norlin *et al*. reported value of 220 kΩ cm². For C4 cold-rolled steel, the polarization resistance (R_p) of the order of 1 kΩ cm² aligns with the values presented in Table 4 for similar steels. The double-layer capacitance of ~100 µF cm^{-2} is reasonable for a bare steel electrode abraded with 600-grit sandpaper. Consistently, the CPE exponent (n) is close to 1 for the Pt electrode and approximately 0.5 for the rough CR4 electrode. These results strongly indicate a correlation between paste electrolyte measurements and those conducted in aerated neutral liquid electrolytes for both noble and active electrodes.

Hard coatings exhibit both high- and low-frequency semicircle responses. Effective capacitances cannot be directly calculated from CPEs due to the overlapping influence of capacitive dispersion from the two semicircles. However, the interplay between circuit elements across different frequencies can still be observed. It must be noted that the following analysis, at frequencies from 10 mHz to 1 nHz, is based on model-derived calculations using the equivalent circuit and parameters from Table 4, rather than on direct experimental measurements. The contribution, % of each circuit element is quantified as the change in impedance resulting from its inclusion in the circuit: $((Z_{without} - Z_{with})/Z_{without})\times100$. Two influences are considered: the effect of CPE1 on the CPE1-(R_{po} -(R_p||CPE2), labelled as X (Figure 9a), and the effect of CPE2 on the (R_p||CPE2), labelled as Y (Figure 9b).

In Figure 9a, for the B1 coating, which demonstrates the best barrier performance with the highest R_{dc} (Table 4), the dominant influence of CPE1 extends to the lowest frequencies. Interestingly, for the A2 coating, which exhibits the poorest barrier performance with the lowest R_{dc} (Table 4), the dominant influence of CPE1 extends the second farthest into the lower frequencies. Despite the very small R_p of A2, the large Q_1 (Table 4) increases the time constant, thereby extending the influence of CPE1 into lower frequencies. However, both R_{po} and R_p are very small in this case (Table 4).

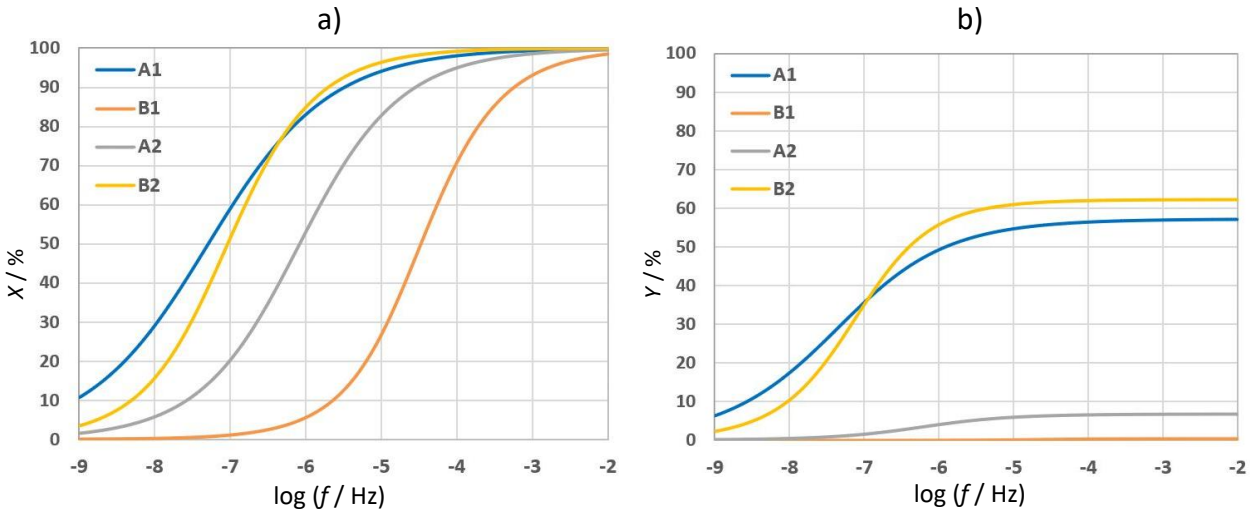

Figure 9. *The percentile influence a) of CPE1 on the modulus of the total CPE1 ∥(R$_{po}$-(CPE2 ∥R$_p$)) circuit impedance and b) of CPE2 on the impedance of the (R$_{po}$-(CPE2 ∥R$_p$) branch in the 10 mHz to 1 nHz frequency range. These results are obtained from model-based calculations using EEC model and data from Table 4*

It is important to note that for polymer coatings, CPE1 is linked to the coating capacitance [51]. However, since hard coatings are not dielectrics but rather electrically conductive and act as barriers due to their inertness, CPE1 is associated with the hard coating/electrolyte double layer rather than the dielectric behaviour of the coating material. Although Q values from Table 4 cannot be directly interpreted as double-layer capacitances, the approximate 10-fold higher Q_1 for the A2 and B2 coatings compared to A1 and B1 can be taken as indicative of greater electrolyte ingress into the coating pores, leading to an increase in the effective coating double-layer surface area.

As CPE1 is positioned in parallel with the (R_{po}-(CPE2∥R_p)) branch, its influence on the overall circuit impedance diminishes at lower frequencies. As a result, the (R_{po}-(CPE2∥R_p)) branch increasingly governs the impedance response in this frequency range. The impedance modulus of this branch is presented in Figure 10 and should be compared with the values of R_{po} and R_p in Table 4. For all coatings, the impedance modulus of the (R_{po}-(CPE2∥R_p)) branch varies between values close to R_{po} at the higher frequency limit and values approaching R_{po}+R_p at the lower frequency limit. The best-performing coating, B1, is the least affected by frequency changes due to the dominance of R_{po}, which is the highest among all coatings (Table 4). The worst-performing coating, A1, is also weakly affected by frequency changes due to the dominance of R_{po}.

Figure 9b presents the percentage contribution of CPE2 to the (R_{po}-(CPE2∥R_p)) branch. Since CPE2 is in parallel with R_p, its diminishing influence accounts for the observed variation in (R_{po}-(CPE2∥R_p)) impedance, transitioning from R_p at high frequencies to R_{po} + R_p in the DC frequency limit. Unlike for CPE1, the CPE2 influence ceases most rapidly for the best barrier coating, which effectively prevents charge accumulation at the substrate/electrolyte interface. For other coatings, CPE2 extends to lower frequencies. Here, the worst coating A2 shows the second-best reach of the CPE2 due to the R_{po} >> R_p,

which acts as a series resistance, modifying how quickly the impedance of the (R_{po}-(CPE2‖R_p)) branch transitions from capacitive to resistive behaviour.

All impedance parameters are normalized to the nominal geometric area. However, the real electrochemically active surface areas are unknown, especially in the case of the exposed substrate, meaning the absolute values of R_p may be underestimated for the best coatings and overestimated for the worst coatings. Therefore, R_p values are not individually analysed. On the other hand, the coatings area is expected to be more consistent among samples, as their surface area is much larger and they are deposited using the same PACVD process, making R_{po} normalization more meaningful than R_p. It can be concluded that R_{po} value plays a crucial role in preventing transition from a coating-dominated response to a substrate-dominated response, making it a key factor in determining the coating efficiency in preventing substrate corrosion.

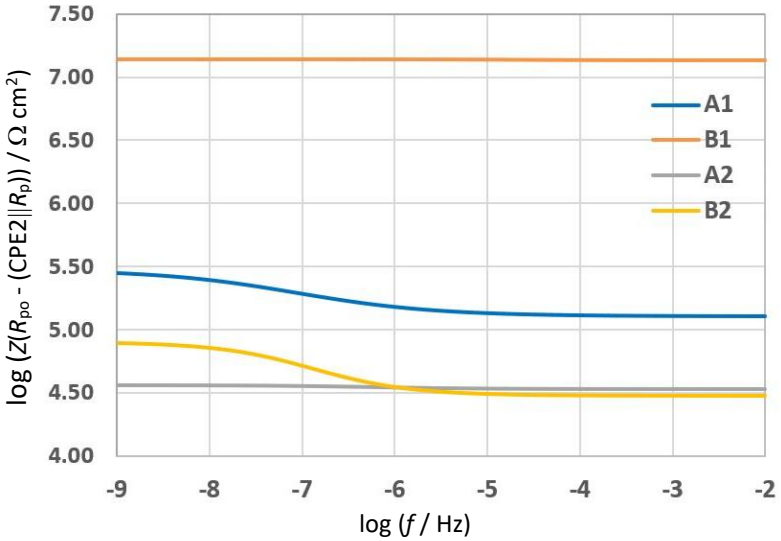

Figure 10. *The impedance modulus of the (*R_{po}*-(CPE2‖*R_p*)) circuit branch in 10 mHz to 1 nHz frequency range. These results are obtained from model-based calculations using EEC model and data from Table 4*

The interpretation of the CPE exponent *n* in this study is grounded in the theoretical framework developed by Hirschorn *et al*. [30], who demonstrated that *n* reflects the distribution of time constants associated with structural or electrochemical inhomogeneity. Specifically, high *n* values (close to 1) are indicative of more ideal capacitive behaviour, typically arising from uniform, compact, and smooth interfaces, while lower *n* values suggest rougher, more porous, or chemically heterogeneous surfaces. Although their analysis was not limited to protective coatings, this foundational model has since been applied widely in interpreting EIS data for coating systems [48].

Accordingly, at high frequencies, the dispersion parameter n_1 of CPE1 determines how closely the coating/electrolyte interface behaves as an ideal capacitor [30]. An n_1 value closer to 1, as observed in B1 and A1, indicates a more uniform coating structure and limited effects of surface roughness and porosity. In contrast, a lower n_1, as seen in B2 and A2, suggests increased dispersion effects, implying a more porous or heterogeneous coating.

The parameter n_1 effectively differentiates between the two coating types (1 and 2). This aligns with first-order histogram parameters, greyscale mean, kurtosis and skewness, which consistently distinguished the coatings. Coating 1 (TiN/TiBN) exhibited a higher proportion of bright pixels, indicating a more organized structure.

At low frequencies, the dispersion parameter n_2 of CPE2 characterizes deviations from ideal capacitive behaviour in the charge transfer process at the substrate/electrolyte interface. A higher n_2,

observed in B1 and B2, indicates a more stable and homogeneous electrochemical interface, where charge transfer is evenly distributed, minimizing the risk of localized corrosion. In contrast, a lower n_2, as seen in A1 and A2, suggests greater electrochemical heterogeneity, leading to uneven charge accumulation, increased susceptibility to localized attack, and a faster transition to active corrosion.

The parameter n_2 effectively differentiates between substrate types A and B. Similarly, the standard deviation of the greyscale mean distinguished the substrates, with substrate A (42CrMo4) producing coatings with a more heterogeneous grayscale distribution, indicative of a less organized structure, potentially reflecting the substrate's influence on coating formation. However, a detailed discussion of this aspect is beyond the scope of this study.

No visible corrosion or coating degradation was detected on any sample following the EIS experiments, either visually, through SEM analysis, or *via* repeated EIS measurements at the same location. This suggests that the short experiment duration and the low corrosivity of the paste electrolyte effectively prevented significant corrosion initiation.

The significant capacitive component of impedance in efficient barrier coatings at low-frequency measurement endpoints can make it challenging to accurately extrapolate impedance to the DC limit using equivalent circuit modelling, *i.e.*, to close the impedance diagram on the real axis [9]. Consequently, the impedance modulus at the lowest measured frequency (0.01 Hz) is often used as an indicator of the protective ability of hard coatings, with higher impedance values signifying better corrosion resistance [51]. The impedance modulus at 0.01 Hz is presented in Table 4. Although the impedance at 0.01 Hz is frequently discussed in the literature as a practical indicator of coating performance, it can significantly underestimate the true DC resistance, especially for highly capacitive systems. It should be noted that R_{dc} is consistently higher than $Z_{0.01\ Hz}$ for all coatings, with the greatest difference observed for B1, reflecting its pronounced capacitive behaviour. For coatings such as B1 in this study, the phase angle remains high at 0.01 Hz, and impedance at this frequency does not reflect the predominantly resistive behaviour at the DC limit. Prior studies with paste electrolyte cells suggest that impedance at 0.01 Hz approximates R_{dc} only when the phase angle is below 30° [33]. Nevertheless, the DC resistance limit (R_{dc}) and the impedance modulus at 0.01 Hz in Table 4 indicate the same ranking of coating barrier efficiency: B1 > A1 > B2 > A2. This ranking is the reverse of the ranking derived from SEM image analysis (A2 > B2 > A1 > B1), which reflects the density of coating grain boundaries. Coatings with a higher grain boundary density exhibit lower barrier performance. While the presence of grain boundaries does not imply direct porosity to the substrate, their surface density, as observed in binarized SEM images, was found to correlate with the electrochemical impedance response. The structural origin or depth of these features was not further explored, as it lies beyond the scope of this study.

In the present paper, a 16-bilayer (32-layer) structure was chosen to ensure adequate multilayer complexity while maintaining practical deposition parameters. Comparable PACVD multilayer coatings with 40 or more individual layers have been reported in the literature [52,53]. The inferior barrier properties of TiN/TiCN coatings (denoted as type 1) can be attributed to their high carbon content, which exceeds the critical concentration of 2.05 at% and likely leads to a high density of defects that compromise coating compactness [53]. Similarly, the lower barrier performance of coatings on the 42CrMo4 substrate (denoted as type A) may be linked to increased coating heterogeneity caused by the substrate, as previously mentioned.

The EIS parameters reported in this study are physically meaningful, and, together with the OCP values, fall within the range presented in Table 3 and the literature data discussed in the introduction. This consistency strengthens the credibility of the investigated method.

Conclusions

The method studied allowed clear differentiation among the coatings analyzed, in the entire range, from poor to excellent. The EIS capacitances and resistances obtained using this method align closely with literature values for similar coating and substrate systems, as well as for cold-rolled steel and platinum reference samples in neutral liquid electrolytes, supporting the credibility of the method.

Additionally, the ranking of coating performance based on total resistance corresponds well with the findings from SE-SEM image analysis, which quantified grain boundary density and homogeneity differences among the coatings. Dense grain boundaries were found to be detrimental to the barrier efficiency of the investigated coatings, as higher grain boundary density correlated with lower total resistance and inferior barrier performance.

The study underlines the importance of a comprehensive approach to EIS analysis of hard coatings that should equally include the resistive and capacitive coating/substrate characteristics which both contribute to reliable coating barrier efficiency evaluation. Current results of the paste electrolyte cell warrant more extensive validation of the proposed method, as it could provide a valuable and practical coating barrier performance screening tool.

Data availability: *Data will be made available on request.*

Declaration of competing Interest: *The authors have stated that they have no financial interests or personal connections that might have impacted the results presented in this paper.*

References

[1] Y. Zhao, H. Zhang, J. Li, X. Liu, Y. Chen, F. Wei, Z. Zhang, Investigating the effect of heat treatment on corrosion resistance of laser-clad NiCrMo coating on mild steel, *Corrosion Science* **229** (2024) 112465. https://doi.org/10.1016/j.corsci.2024.112465

[2] W. Tang, S. Wang, S. Li, S. Yu, X. Yuan, C. Yang, J. Zhang, Y. Gao, Research progress on coating and coating technology of fuel cell metallic bipolar plate, *Next Materials* **4** (2024) 100062. https://doi.org/10.1016/j.nxmate.2023.100062

[3] M. Kumar, R. Kumar, S. Kumar, Coatings on orthopedic implants to overcome present problems and challenges: A focused review, *Materials Today Proceedings* **45** (2021) 5269-5276. https://doi.org/10.1016/j.matpr.2021.01.831

[4] M.K. Hirschfeld, C. Pfohl, K.-T. Rie, J.W. Schultze, Corrosion properties of titanium-based hard coatings on steel, *Materials Science and Engineering Technology* **29** (1998) 484-495. https://doi.org/10.1002/mawe.19980290907

[5] J.C. Caicedo, G. Cabrera, H.H. Caicedo, C. Amaya, W. Aperador, Nature in corrosion-erosion surface for [TiN/TiAlN]n nanometric multilayers growth on AISI 1045 steel, *Thin Solid Films* **520** (2012) 4350-4361. https://doi.org/10.1016/j.tsf.2012.02.061

[6] I. Milošev, H.H. Strehblow, B. Navinšek, M. Metikoš-Huković, Electrochemical and thermal oxidation of TiN coatings studied by XPS, *Surface and Interface Analysis* **23** (1995) 529-539. https://doi.org/10.1002/sia.740230713

[7] H. Olia, R. Ebrahimi-Kahrizsangi, F. Ashrafizadeh, I. Ebrahimzadeh, Corrosion study of TiN, TiAlN and CrN multilayer coatings deposited on martensitic stainless steel by arc cathodic physical vapour deposition, *Materials Research Express* **6** (2019) 046425. https://doi.org/10.1088/2053-1591/aaff11

[8] P.M. Perillo, Corrosion behavior of coatings of titanium nitride and titanium-titanium nitride on steel substrates, *Corrosion* **62** (2006) 182-185. https://doi.org/10.5006/1.3278263

[9] Y. Massiani, A. Medjahed, P. Gravier, L. Argème, L. Fedrizzi, Electrochemical study of titanium nitride films obtained by reactive sputtering, *Thin Solid Films* **191** (1990) 305-316. https://doi.org/10.1016/0040-6090(90)90382-N
[10] R. Ali, Corrosion behavior of titanium-based ceramic coatings deposited on steels, PhD Thesis, Technischen Fakultät der Universität Erlangen-Nürnberg, 2016. https://open.fau.de/handle/openfau/7027
[11] A. Ali, A. Ahmad, K.M. Deen, Impeding corrosion of sintered NdFeB magnets with titanium nitride coating, *Materials and Corrosion* **61** (2010) 130-135. https://doi.org/10.1002/maco.200905265
[12] B. Avcı, K. Kazmanlı, B. Evren, M. Ürgen, Contribution of galvanic coupling with TiN, TiAlN, and CrN to the corrosion of steel in neutral and acidic chloride solutions, *Materials and Corrosion* **74** (2023) 1390-1399. https://doi.org/10.1002/maco.202313848
[13] C. Outen, D.W. Konopka, T.F. Fennessey, Development of Titanium Nitride Fractal Coatings for Cardiac and Neural Electrostimulation Electrodes, *SVC Digital Library* (2015) 33-37. https://doi.org/10.14332/SVC14.PROC.1819
[14] B. Subramanian, K. Ashok, K. Subramanian, D. Sastikumar, G. Selvan, M. Jayachandran, Evaluation of corrosion and wear resistance of titanium nitride (TiN) coated on mild steel (MS) with brush plated nickel interlayer, *Surface Engineering* **25** (2009) 490-495. https://doi.org/10.1179/026708408X330621
[15] B. Matthes, E. Broszeit, J. Aromaa, H. Ronkainen, S.-P. Hannula, A. Leyland, A. Matthews, Corrosion performance of some titanium-based hard coatings, *Surface and Coatings Technology* **86-87** (1996) 307-314. https://doi.org/10.1016/0257-8972(91)90105-6.
[16] M. A. M. Ibrahim, S. F. Korablov, M. Yoshimura, Corrosion of stainless steel coated with TiN, (TiAl)N and CrN in aqueous environments, *Corrosion Science* **44** (2002) 815-828. https://doi.org/10.1016/S0010-938X(01)00102-0
[17] B. Elsener, A. Rota, H. Böhni, Impedance study on the corrosion of PVD and CVD titanium nitride coatings, *Materials Science Forum* **44-45** (1991) 29-38. https://doi.org/10.4028/www.scientific.net/MSF.44-45.29
[18] A. Kameneva, V. Kichigin, N. Lobov, N. Kameneva, Effect of structure, elemental and phase composition gradient of nitride multilayer coatings on corrosion protection of different substrates in 3% NaCl and 5% NaOH solutions, *Data in Brief* **27** (2019) 104796. https://doi.org/10.1016/j.dib.2019.104796
[19] R. Ali, E. Alkhateeb, F. Kellner, S. Virtanen, N. Popovska-Leipertz, Chemical vapor deposition of titanium-based ceramic coatings on low carbon steel: Characterization and electrochemical evaluation, *Surface and Coatings Technology* **205** (2011) 5454-5463. https://doi.org/10.1016/j.surfcoat.2011.06.014
[20] J. F. Correa, J. C. Caicedo, W. A. Aperador, Comparison of structural and electrochemical properties among TiCN, BCN, and CrAlN coatings under aggressive environments, *Journal of Materials Engineering and Performance* **30** (2021) 3586-3602. https://doi.org/10.1007/s11665-021-05691-7
[21] J. J. O. Florez, Y. L. C. Godoy, S. E. R. Posada, Resistencia a la corrosión de recubrimientos de nitruros metálicos depositados sobre acero AISI M2, *Ingeniería y Desarrollo* **30** (2012) 1-22. (In Spanish) https://www.redalyc.org/pdf/852/85223369002.pdf
[22] M. Azizi-Malekabadi, H. Bakhshi, H. Shahbazi, H. Nosrati, Enhancement of the Ti-6Al-4V alloy corrosion resistance by applying CrN/CrAlN multilayer coating *via* Arc-PVD method, *International Journal of Applied Ceramic Technology* **18** (2021) 1288-1296. https://doi.org/10.1111/ijac.13763
[23] R. Kalnina, V. Priednieks, K. Lukins, A. Gasparjans, A. Rijkure, Corrosion and electrochemical impedance spectroscopy of thin TiALN and TiCN PVD coatings for protection of ballast

water screen filters, *Latvian Journal of Physics and Technical Sciences* **58** (2021) 64-78. https://doi.org/10.2478/lpts-2021-0012

[24] D. Landek, S. Jakovljević, V. Alar, S. Kovačić, Effect of steel substrate on the corrosion properties of a gradient multilayer TiN/TiCN coating deposited by the PACVD process, *Materials and Corrosion* **70** (2019) 307-318. https://doi.org/10.1002/maco.201810358

[25] E. Alkhateeb, R. Ali, S. Virtanen, N. Popovska, Electrochemical evaluation of the corrosion behavior of steel coated with titanium-based ceramic layers, *Surface and Coatings Technology* **205** (2011) 3006-3011. https://doi.org/10.1016/j.surfcoat.2010.11.007

[26] Ş. Danışman, D. Odabaş, M. Teber, The effect of TiN, TiAlN, TiCN thin films obtained by reactive magnetron sputtering method on the wear behavior of Ti6Al4V alloy: A comparative study, *Coatings* **12** (2022) 1238. https://doi.org/10.3390/coatings12091238

[27] F. Jasempoor, H. Elmkhah, O. Imantalab, A. Fattah-alhosseini, Improving the mechanical, tribological, and electrochemical behavior of AISI 304 stainless steel by applying CrN single layer and Cr/CrN multilayer coatings, *Wear* **504-505** (2022) 204425. https://doi.org/10.1016/j.wear.2022.204425

[28] Ç. Çomaklı, Improved structural, mechanical, corrosion, and tribocorrosion properties of Ti45Nb alloys by TiN, TiAlN monolayers, and TiAlN/TiN multilayer ceramic films, *Ceramics International* **47** (2021) 4149-4156. https://doi.org/10.1016/j.ceramint.2020.09.292.

[29] F. Mansfeld, Electrochemical Impedance Spectroscopy (EIS) as a new tool for investigating methods of corrosion protection, *Electrochimica Acta* **35** (1990) 1533-1544. https://doi.org/10.1016/0013-4686(90)80007-B

[30] B. Hirschorn, M. E. Orazem, B. Tribollet, V. Vivier, I. Frateur, M. Musiani, Determination of effective capacitance and film thickness from constant-phase-element parameters, *Electrochimica Acta* **55** (2010) 6218-6227. https://doi.org/10.1016/j.electacta.2009.10.065

[31] I. Bera, I. Bašurić, I. Šoić, S. Martinez, Investigating the impact of post-weld cleaning and passivation on the performance of austenitic stainless steel using an EIS paste-electrolyte cell, *Journal of Solid State Electrochemistry* **28** (2024) 2827-2836. https://doi.org/10.1007/s10008-024-05849-y

[32] I. Bera, I. Šoić, S. Kurajica, S. Martinez, Innovative comparative EIS study of weathering steel: 2-year and 44-year-old, natural and artificial patinas, *Electrochimica Acta* **498** (2024) 144624. https://doi.org/10.1016/j.electacta.2024.144624

[33] I. Šoić, I. Šoljić, M. Eškinja, A. Mujezinović, S. Martinez, The novel paste electrolyte measuring cell for EIS testing of the commonly used surface protection on bronze, *Progress in Organic Coatings* **177** (2023) 107442. https://doi.org/10.1016/j.porgcoat.2023.107442

[34] K. Baba, R. Hatada, Corrosion-resistant titanium nitride coatings formed on stainless steel by ion-beam-assisted deposition, *Surface and Coatings Technology* **66** (1994) 368-372. https://doi.org/10.1016/0257-8972(94)90032-9

[35] M. P. Nikolova, S. Valkov, R. Iosub, E. Yankov, P. Petrov, Electrochemical impedance spectroscopy of complex titanium nitride coating with thin surface oxide film deposited on pure titanium, *Revue de Chimie (Bucharest)* **70** (2019) 42-50. https://solacolu.chim.upb.ro/p42-50.pdf

[36] Z. Weiß, K. Marshall, Elemental depth profiling of coated and surface-modified materials by GD-OES: hard coatings on cutting tools, *Thin Solid Films* **308-309** (1997) 382-388. https://doi.org/10.1016/S0040-6090(97)00586-5

[37] I. Von Bradke, F. Gitzhofer, R. Henne, Porosity determination of ceramic materials by digital image analysis - a critical evaluation, *Scanning* **27** (2005) 132-135. https://doi.org/10.1002/sca.4950270305

[38] I. Jastrzębska, A. Piwowarczyk, Traditional vs. automated computer image analysis - a comparative assessment of use for analysis of digital SEM images of high-temperature ceramic material, *Materials* **16** (2023) 812. https://doi.org/10.3390/ma16020812
[39] Y. Y. Tan, K. S. Sim, C. P. Tso, A study on central moments of the histograms from scanning electron microscope charging images, *Scanning* **29** (2007) 211-218. https://doi.org/10.1002/sca.20065
[40] T. Prill, C. Redenbach, D. Roldan, M. Godehardt, K. Schladitz, S. Höhn, Simulating permeabilities based on 3D image data of a layered nano-porous membrane, *International Journal of Solids and Structures* **184** (2020) 3-13. https://doi.org/10.1016/j.ijsolstr.2019.04.010
[41] S. H. R. Sanei, R. S. Fertig, Uncorrelated volume element for stochastic modeling of microstructures based on local fiber volume fraction variation, *Composites Science and Technology* **117** (2015) 191-198. https://doi.org/10.1016/j.compscitech.2015.06.010
[42] D. Y. Kim, S. Y. Yoon, S. Y. Choi, Microstructure and properties of titanium nitride coatings deposited on tool steels by PACVD process, *Journal of Ceramic Processing Research* **22** (2021) 1579-1585. http://www.jcpr.or.kr/journal/archive/view/1579
[43] C. A. Schneider, W. S. Rasband, K. W. Eliceiri, NIH Image to ImageJ: 25 years of image analysis, *Nature Methods* **9** (2012) 671-675. https://doi.org/10.1038/nmeth.2089
[44] A. R. Naghashzadeh, A. Shafyei, F. Sourani, Nanoindentation and tribological behavior of TiN-TiCN-TiAlN multilayer coatings on AISI D3 tool steel, *Journal of Materials Engineering and Performance* **31** (2022) 4335-4342. https://doi.org/10.1007/s11665-021-06533-2
[45] M. Mirzaee-Sisan, H. Khorsand, M. H. Siadati, Effects of duty cycle on nanostructured TiN coatings on AISI H11 and AISI D2 steels, *Journal of Bio- and Tribo-Corrosion* **10** (2024) 56. https://doi.org/10.1007/s40735-024-00856-y
[46] P. Perumal, K. Ramanathan, L. Ganesan, B. Subramanian, V. Ganesh, B. Stalin, Investigation of TiN coating uniformity and its corrosion behaviour using image processing, *Materials Research Express* **16** (2019) 046411. https://doi.org/10.1088/2053-1591/aafae9
[47] C. H. Li, C. K. Lee, Minimum cross entropy thresholding, *Pattern Recognition* **26** (1993) 617-625. https://doi.org/10.1016/0031-3203(93)90115-D
[48] A. M. G. Ferreira, M. L. Zheludkevich, M. G. S. Ferreira, Determination of resistivity profiles in anti-corrosion coatings from impedance spectroscopy, *Progress in Organic Coatings* **76** (2013) 733-740. https://doi.org/10.1016/j.porgcoat.2013.01.011
[49] B. N. Grgur, V. Lazić, D. Stojić, R. Rudolf, Electrochemical testing of noble metal dental alloys: The influence of their chemical composition on the corrosion resistance, *Corrosion Science* **184** (2021) 109412. https://doi.org/10.1016/j.corsci.2021.109412
[50] A. Norlin, J. Pan, C. Leygraf, Investigation of interfacial capacitance of Pt, Ti and TiN coated electrodes by electrochemical impedance spectroscopy, *Biomolecular Engineering* **19** (2002) 67-71. https://doi.org/10.1016/S1389-0344(02)00013-8
[51] Q. Wang, F. Zhou, Z. Zhou, L. K.Y. Li, J. Yan, Electrochemical performance of TiCN coatings with low carbon concentration in simulated body fluid, *Surface and Coatings Technology* **253** (2014) 199-204. https://doi.org/10.1016/j.surfcoat.2014.05.037
[52] S. Kovačić, F. Cajner, D. Landek, Wear Resistance of TiN/TiCN and TiN/TiBN Multilayer Coatings Applied on Hot Work Tool Steel, *Key Engineering Materials* **674** (2016) 257-262. https://doi.org/10.4028/www.scientific.net/KEM.674.257
[53] D. Landek, S. Jakovljević, J. Jačan, Increasing the Wear Resistance of High-alloy Tool Steels for Cold Work with Multilayer Coatings TiN/TiCN and TiN/Ti-B-N Applied by the PACVD Process, *Berg- und Hüttenmännische Monatshefte* **168 (3)** (2023) 120-129. (In German) https://doi.org/10.1007/s00501-023-01329-4

[54] F. Mansfeld, Use of electrochemical impedance spectroscopy for the study of corrosion protection by polymer coatings, *Journal of Applied Electrochemistry* **25** (1995) 3. http://link.springer.com/10.1007/BF00262955